PERGAMON

Solid-State Electronics 45 (2001) 1577–1589

SOLID-STATE ELECTRONICS

High-Q microphotonic electro-optic modulator

D.A. Cohen, M. Hossein-Zadeh, A.F.J. Levi *

Department of Electrical Engineering, University of Southern California, Denny Research Building 118, Los Angeles, CA 90089-1111, USA

Received 28 January 2001; accepted 29 March 2001

Abstract

A microphotonic mm-wave modulator using simultaneous RF and optical resonance in an electro-optic medium is presented. Theory and simulation of modulator operation is discussed, and experimental results demonstrating modulation using simultaneous resonance in the mm-wave range are reported. © 2001 Elsevier Science Ltd. All rights reserved.

Keywords: mm-wave receiver; $LiNbO_3$ modulator; Resonant detection; Microphotonic; Microdisk; Microsphere; Resonator

1. Introduction

The wide-scale implementation of microwave cellular telephone networks, and continued need for personal data assistants (PDAs) is driving development of indoor wireless and microcell wireless systems [1]. Recently, a microphotonic modulator for a novel wireless and front-end RF receiver architecture operating at mm-wave frequencies was proposed [2]. Previous work has focused on modulator development and demonstration of efficient modulation at microwave frequencies [3,4]. In this paper, we present initial experimental results demonstrating modulation at mm-wave frequencies by achieving simultaneous resonance of RF and microphotonic electro-optic resonators. In addition, results of simulations describing optical modulation within the microphotonic resonator are presented.

2. $LiNbO_3$ microphotonic resonator

A microphotonic optical resonator is fabricated from an electro-optic material. In the work presented here, we use a z-cut $LiNbO_3$ disk-shaped resonator with optically polished curved side walls. The index of refraction along the extraordinary axis (z-axis) is $n_{opt} = 2.14$ at an optical wavelength $\lambda = 1.5$ μm, and greater than 5.1 at RF frequencies in the mm-wave regime [5]. Simultaneous resonance between optical and RF fields is possible inside the disk. The optical field is resonant within the microphotonic modulator by confining a TE-polarized optical-field in a high quality-factor (Q) whispering-gallery mode (WGM) along the periphery of the disk, while metal electrodes feed RF power from a resonant electrical circuit. The optical resonator's large Q increases the effective interaction length of photons in the electro-optic material. In addition, a simultaneously resonant RF electrical feed for voltage enhancement and a patterned electrode structure provides high-sensitivity at mm-wave frequencies.

Fig. 1(a) shows the basic geometry of the $LiNbO_3$ resonator. These devices are disks of radius R, where $1 \leqslant R \leqslant 3$ mm, and thickness d, where $0.2 \leqslant d \leqslant 1$ mm. The side wall of the disk is optically polished with a radius of curvature, R'. In this work $R = R'$. The equator of the disk's curved side wall should be accurately maintained at height $d/2$. A photograph of a larger device is shown in Fig. 1(b) to illustrate the optically polished curved sidewalls of the resonator.

2.1. Solving for optical resonances in the microphotonic resonator

WGMs in disk-shaped dielectric resonators arise from solution of Maxwell's equations. The large dielectric

* Corresponding author. Tel.: +1-213-740-7318; fax: +1-213-740-9280.

E-mail address: alevi@usc.edu (A.F.J. Levi).

PII: S0038-1101(01)00165-4

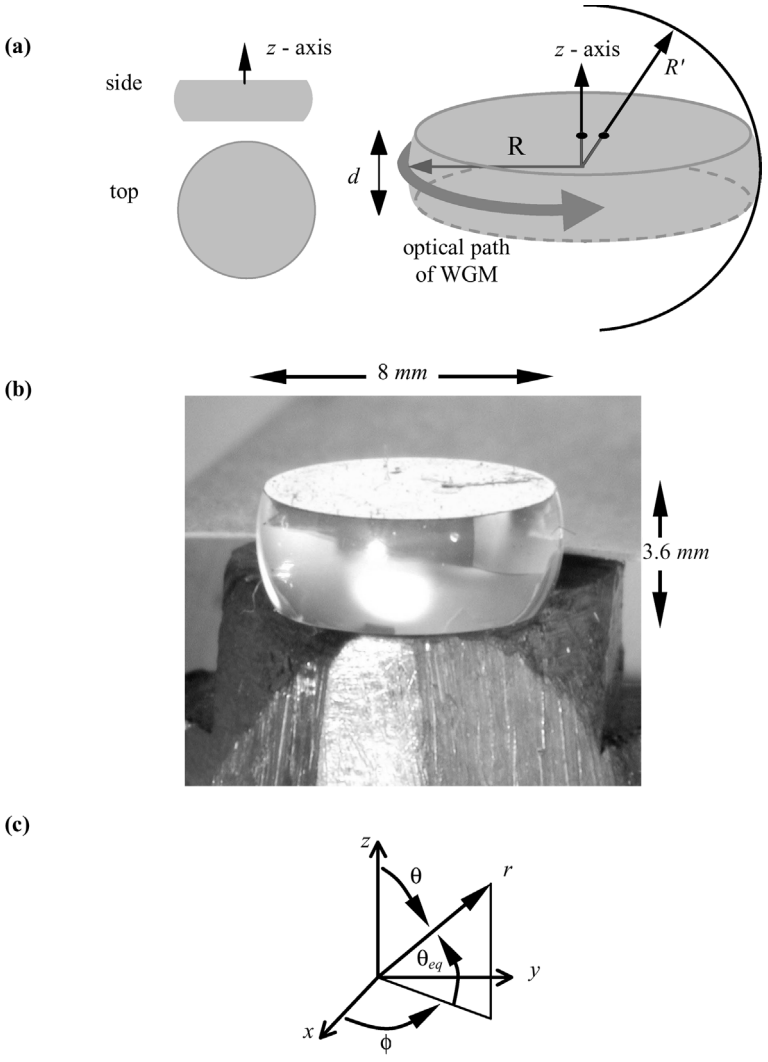

Fig. 1. (a) Geometry of a microdisk indicating disk radius R, disk thickness d and curved side walls with radius of curvature R'. (b) Photograph of a large z-cut $LiNbO_3$ disk-shaped resonator with solid-gold top and bottom flat-electrodes and optically polished curved side walls mounted on a ground plane. (c) The coordinate system used to solve the electromagnetic modes of a spherical resonator.

discontinuity between air and resonator result in electromagnetic resonances which in the ray-tracing approximation are explained by total internal reflection. When the disk radius R is equal to R', the electromagnetic solutions to the disk resonator are found by defining the disk to be a sphere with part of the top and bottom hemispheres removed. Therefore, the nature of WGMs propagating within the disk is essentially the same as modes that propagate within passive dielectric microspheres. The only exception is that some higher-order modes are spatially filtered by losses introduced at the top and bottom disk interfaces. Whispering gallery resonances are characterized by high electric-field intensity close to the air–dielectric interface and very high-Q. Loss due to finite curvature becomes small when the resonator dimension is significantly greater than the optical resonance wavelength. Hence, for optical wavelengths near $\lambda = 1.55$ μm, the Q of optical dielectric resonators greater than ~10 m in diameter is typically limited by attenuation due to scattering from surface imperfections.

The problem of electromagnetic oscillation in a dielectric sphere has been solved explicitly for a lossless, linear medium with no sources [6]. Assuming monochromatic solutions of the form $\mathbf{E}(\mathbf{r},t) = \mathbf{E}(\mathbf{r})e^{-i\omega t}$ the vector Helmholtz equation is

$$\nabla^2\mathbf{E}(\mathbf{r}) + \mu\varepsilon\frac{\omega^2}{c^2}\mathbf{E}(\mathbf{r}) = 0$$

where ε and μ are the relative permitivity and permeability, and $\omega = 2\pi f$, where f is the frequency of the electric-field oscillation. We would like to express the vector $\mathbf{E}$ in terms of radial (E_r), meridional (E_θ), and azimuthal (E_ϕ) components. However, the Laplacian of the vector $\mathbf{E}$ results in three partial differential equations each involving E_r, E_θ, and E_ϕ. Hence, the simple separation of the Helmholtz equation in the rectangular coordinate system does not occur in the spherical coordinate system. It can be shown that three solutions in terms of the field ψ are

$$\mathbf{E} = (\nabla\psi)$$

$$\mathbf{E}_{\mathrm{TE}} = (\mathbf{r}\times\nabla\psi)$$

$$\mathbf{E}_{\mathrm{TM}} = \frac{\mathrm{i}c}{\omega}\nabla\times(\mathbf{r}\times\nabla\psi)$$

These are also independent vector solutions which result in three separable partial differential equations. Using these solutions, the scalar Helmholtz equation is solved for ψ, where the scalar equation is given by

$$\nabla^2\psi + \mu\varepsilon\frac{\omega^2}{c^2}\psi = 0$$

The solutions $\mathbf{E}_{\mathrm{TE}}$ and $\mathbf{E}_{\mathrm{TM}}$ are those of interest for electromagnetic WGM solutions excited by evanescent coupling along the equator of the sphere. The first is named the transverse electric (TE) solution because $\mathbf{E}_{\mathrm{TE}}$ is tangent to the spherical surface, while the second is the transverse magnetic (TM) solution because the magnetic field $\mathbf{H}_{\mathrm{TM}}$ is tangent to the spherical surface [7]. This notation is opposite to that used with microdisk lasers [8] where TE polarization is along the radial unit vector. The microdisk laser definition comes from multiple quantum well slab-waveguide geometries.

Although the Helmholtz equation can be solved explicitly for the dielectric sphere, a simplification is achieved by assuming the electromagnetic field polarization may be approximated as constant along one coordinate axis [9]. In this case, the TE and TM modes are redefined as those with vector electric-field components

$$\mathbf{E}_{\mathrm{TM}} = \hat{\boldsymbol{\theta}}E_\theta \equiv \hat{\boldsymbol{\theta}}\Psi$$

$E_r = E_\phi = 0$, and TM modes defined as those with vector magnetic field components

$$\mathbf{H}_{\mathrm{TM}} = \hat{\boldsymbol{\theta}}H_\theta \equiv \hat{\boldsymbol{\theta}}\Psi$$

$H_r = H_\phi = 0$. The validity of this approximation has been confirmed numerically by Little et al. [9].

Such an approximation permits separation of the vector Helmholtz equation as seen with rectangular coordinates. Again starting with the vector Helmholtz equation, and using the definitions for $\mathbf{E}_{\mathrm{TE}}$ ($\mathbf{H}_{\mathrm{TM}}$) above, the resulting scalar equation

$$\nabla^2\psi + \mu\varepsilon\frac{\omega^2}{c^2}\psi = 0$$

is easily solved in the spherical coordinate system. Boundary conditions are then applied to obtain the characteristic equations and normalization constants.

By imposing boundary conditions at the disk radius R_0 and restricting the spherical Bessel function from diverging at the origin, one obtains

$$\mathbf{E}_{\mathrm{TE}}(\mathbf{H}_{\mathrm{TM}}) = \sum\psi(r,\theta,\phi) = \sum_{lm}\psi_r^l(r)Y_{lm}(\theta,\phi)$$

$$\psi_r^l(r) \propto j_l(kr), \quad r \leqslant R_0$$

$$\psi_r^l(r) \propto \mathrm{e}^{-\alpha_s(r-R_0)}, \quad r > R_0$$

where $j_l(kr)$ are spherical Bessel function, Y_{lm} are spherical harmonics, and l and m are eigenvalues solved from boundary conditions. The exponential decay defines only the bound portion of the field outside the sphere. Radiation modes are ignored. In the equations above $k = 2n_s/\lambda$, where n_s is the refractive index of the sphere, and λ is the electromagnetic wavelength in free space. The third eigenvalue n is found from the characteristic equations resulting from the boundary condition that the interior and exterior tangential fields at the surface of sphere must be equal.

From these solutions, we find the eigenmodes of the microresonator are characterized by polarization (TE or TM), and the three eigenvalues n, l, and m. The radial eigenvalue $n \gg 1$ is the number of field maxima in the direction of the sphere radius, l is approximately the number of wavelengths that fit into the optical length of the resonator, and m is the number of field maxima in the equatorial plane. We will show later that the number of polar intensity maxima is $l - m + 1$.

We see that as $l = m$ increases, the optical power begins to concentrate closer to the equator. The longitudinal cross-section of the x–z plane displays the concentration of field toward both the equator and disk edge as l and m increase. A cross-section of the mode in the x–y plane demonstrates the increase in number of field maxima, and a trend in which the mode becomes increasingly confined to the disk edge.

A significant approximation can be made with the angular distribution of the mode along the polar axis [10]. We define a new coordinate $\theta_{\mathrm{eq}} = \theta - \pi/2$, such that $\theta_{\mathrm{eq}} = 0$ along the equator as shown in Fig. 1(c). Making the approximations $\theta_{\mathrm{eq}} \ll 2\pi$ and $m \gg 1$, and

including this in the polar differential equation, $\psi_\theta(\theta_{eq})$ becomes

$$\psi_\theta(\theta_{eq}) \propto e^{-m/2\theta_{eq}^2} H_N(\sqrt{m}\theta_{eq})$$

$$N = l - m$$

where $H_N(x)$ are the Hermite polynomials, with $H_0(x) = 1, H_1(x) = 2x$, $H_2(x) = 4x^2 - 2$, etc. For case of large m, and $l \approx m$ the resulting WGM is Gaussian in nature. From this approximation, and the nature of Hermite polynomials, we see that there are $l - m + 1$ polar intensity maxima. At $l - m = 0$, the mode is Gaussian and centered about the equator. As $l - m$ increases, the energy distribution spreads further from the equator. Because input laser light typically has a Gaussian beam profile, we expect that the $l = m$ Gaussian modes are those that are most strongly coupled [10]. In addition, in a perfect sphere, WGM frequencies depend only on n and l, and hence are $2m + 1$ degenerate in frequency. However, in any sphere with finite ellipticity this degeneracy is broken [11].

Fig. 2 shows the simulated WGM power distribution for disks typical of that used in experimentation. Fig. 2(a) shows the normalized radial profile of the spherical Bessel function with $n = 1$ for a 2.0 mm ($l = 8690$), 3.5 mm ($l = 15120$), and 5.84 mm ($l = 25260$) disk. By approximating the boundary condition at the disk radius to be $\mathbf{E}_{TE}(R) = 0$, the full width half maximum (FWHM) of the modes along the radius are 2.6, 3.7, and 4.8 μm for the 2.0, 3.5, and 5.84 mm disks, respectively. Normalized profile along the z-axis for $N = l - m = 0$, 1, 2, and 3 for a 2.0, 3.5, and 5.84 mm disk are plotted in Fig. 2(b). These figures demonstrate that the relative angular distribution of the mode increases with decreasing disk radius, but the actual mode height along the z-axis decreases.

Fig. 3(a) shows the two-prism evanescent coupling scheme used to couple light into and out of the disk. When TE-polarized WGM modes are excited within the $LiNbO_3$ microphotonic resonator the detected optical spectrum shows peaks corresponding to the free spectral range (FSR) of the resonant cavity. This FSR is defined as $\Delta f_{FSR} \approx c/(n_{opt} 2\pi R)$, where n_{opt} is the optical refractive index, and R is the radius of the disk. It should be noted that $1/\Delta f_{FSR}$ is equal to the round trip time of the cavity $\tau_{disk} = (n2\pi R)/c$. Results using a tunable DFB laser to scan the entire FSR of the disk are shown in Fig. 3(b) for a disk of diameter $2R = 5.85$ mm, and thickness

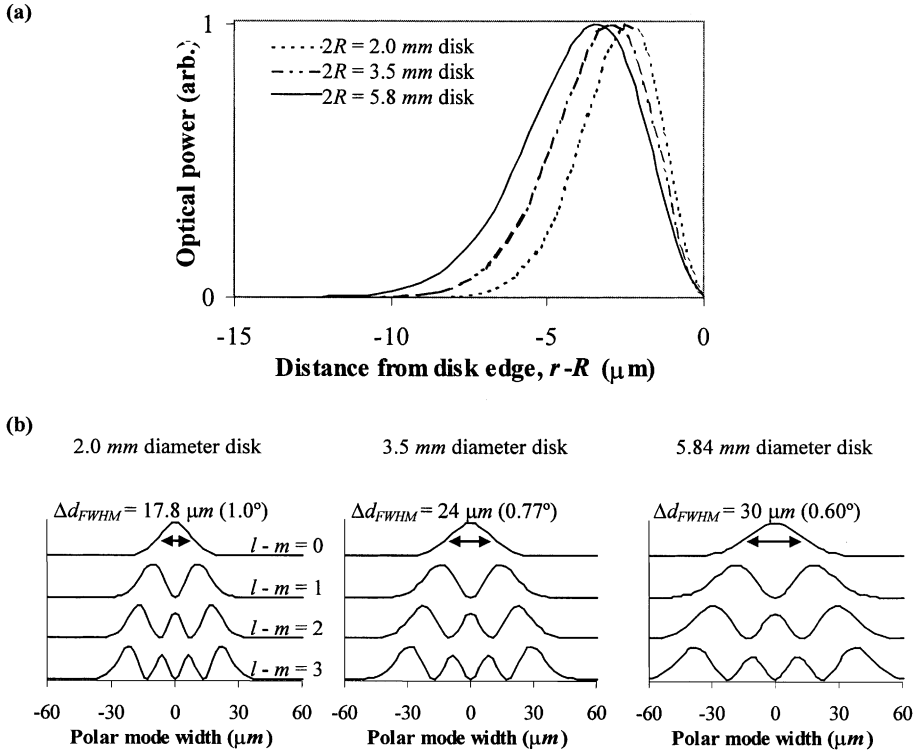

Fig. 2. WGM power distribution for disks of large $l = m$. (a) Normalized profile of spherical Bessel functions with $\eta = 1$ for a 2.0 mm ($l = 8690$), 3.5 mm ($l = 15120$), and 5.84 mm ($l = 25260$) disk. The FWHM of the modes are 2.6, 3.7 and 4.8 μm for the 2.0, 3.5 and 5.84 mm disks, respectively. (b) Normalized profile of spherical harmonics using Hermite polynomial approximation for $N = l - m = 0$, 1, 2, and 3 for a 2.0, 3.5, and 5.84 mm disk.

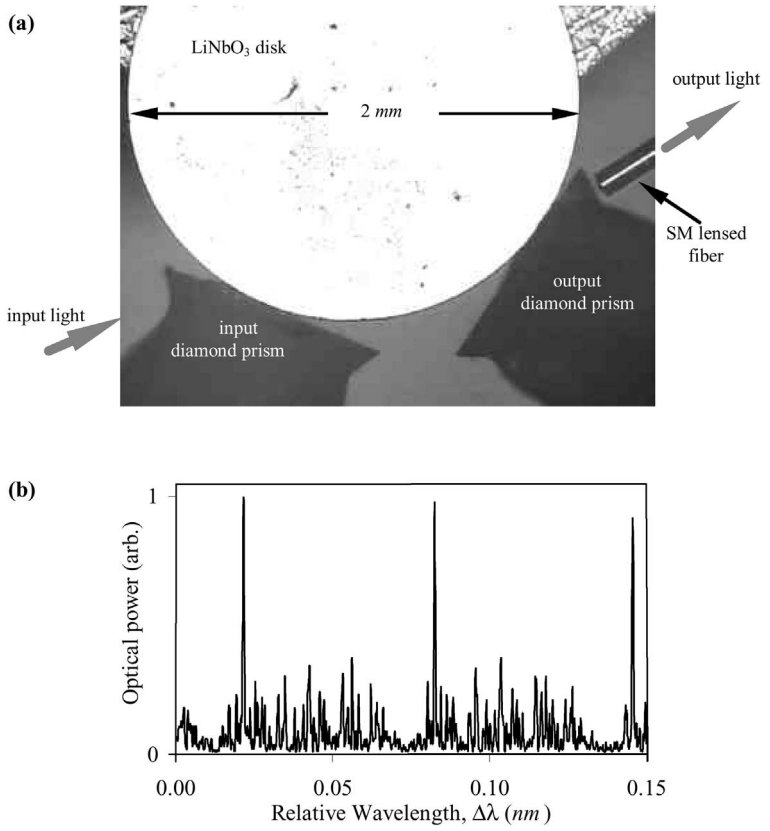

Fig. 3. (a) Top view of two prism coupling using diamond prisms. Input light is coupled into the prism on the right. Light output from the disk is collected at the single mode fiber output coupler. (b) Optical spectrum for TE polarized light when alignment is optimized for single optical mode excitation with FSR = 7.57 GHz, and $Q > 4 \times 10^6$. The disk used has a diameter 5.85 mm and thickness of 0.7 mm. Wavelength of lasing light is 1.55 μm.

$d = 0.74$ mm. This disk exhibited a FSR of 7.57 GHz (60.6 pm) for TE optical modes with WGM optical Q greater than 4.1×10^6.

2.2. Electro-optic modulation configuration and theory

Fig. 4(a) shows the schematic diagram of the experimental approach. An RF input signal is incident on the modulator electrodes. This mm-wave signal feeds the electrodes of the microphotonic resonator where the RF signal is directly converted via the electro-optic response of the modulator to an optical signal with a 200 THz optical carrier frequency supplied by a DFB laser. By patterning metal electrodes periodically about the disk circumference, it is possible to obtain a resonant opto-electronic modulation response at large RF frequencies. Photons make a number of round trips in the resonator, thereby interacting with the RF field on multiple passes which increase the total phase shift seen by any individual photon. This results in improved sensitivity to the applied RF field. The resulting phase-modulated optical signal may be converted to amplitude modulation through use of a standard Mach–Zehnder configuration. The intensity of the amplitude-modulated optical carrier is detected using an optical receiver whose response is sensitive only to base-band frequencies.

Basic principles regarding the coupling of photons into and out of the microphotonic resonator can be understood through a directional coupler approach. Fig. 5 shows the generic approach to model the coupling of light from any evanescent coupler (e.g. prism) into a disk or ring structure. Input light is incident on coupling region 1 with an electric-field coupling coefficient $i\kappa_1$ and output from coupling regions 1 and 2 with electric-field coupling coefficients $i\kappa_1^*$ and $i\kappa_2^*$, respectively. Single prism coupling is defined when monitoring output 1 with $\kappa_2 = 0$, and two prism coupling when monitoring output 2 with $\kappa_2 \neq 0$.

Using the steady-state loop approach [11], A_1 is defined as the steady state electric-field amplitude for input light entering coupling region 1, B_1 is the field exiting coupling region 1, and A_2 and B_2 are the fields inside the

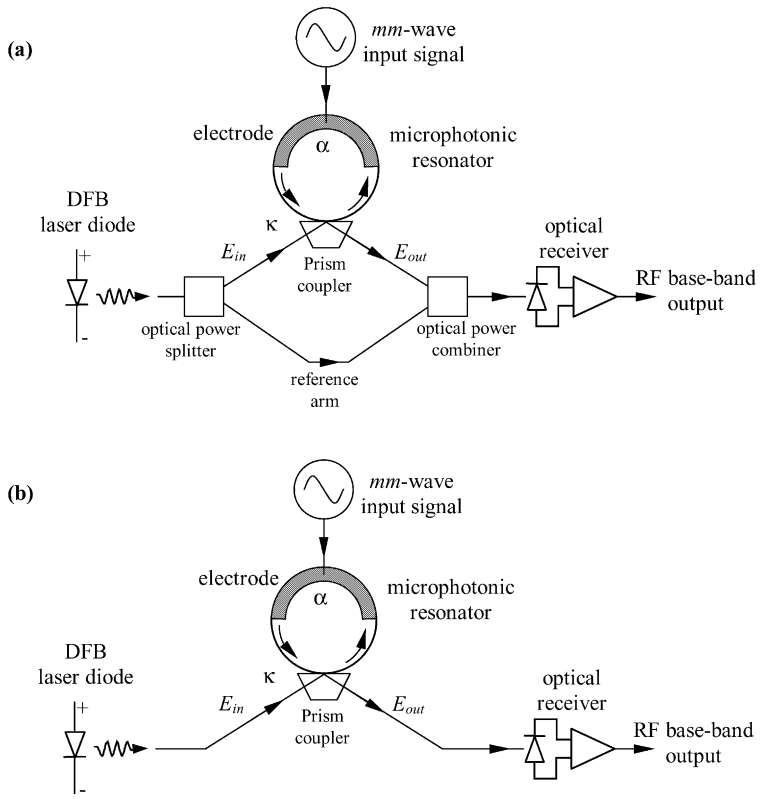

Fig. 4. (a) Schematic showing the receiver proposed for mm-wave RF detection. An electromagnetic wave received at a RF antenna feeds electrodes of the microphotonic modulator. The modulator directly converts the RF signal to an optical carrier via the electro-optic effect. The resulting phase-modulated optical signal is converted to amplitude modulation through the use of a standard Mach–Zehnder configuration. (b) Schematic showing the receiver proposed for mm-wave RF detection without the need of a Mach–Zehnder reference arm. The phase-modulated optical signal is internally converted to amplitude modulation through interference with previous optical round trips.

resonator before and after coupling region 1. Similarly, D_1 is the field exiting coupling region 2, and C_2 and D_2 are the fields inside the resonator before and after coupling region 2. For simplicity, a lossless symmetric coupler is assumed, with field coupling constant $i\kappa_1 = -\mathrm{i}\kappa_1^*$ in region 1, and $\mathrm{i}\kappa_2$ in region 2. The transmission coefficient $T_{A_1B_1}$ from A_1 to B_1 is $T_{A_1B_1} = (1-\kappa_1^2)^{1/2}$. In the case of the prism coupler, the coupling coefficient κ is a function of gap spacing, coupler geometry, and disk size.

The round-trip disk electric optical field transmission coefficient $\alpha = \alpha_1\alpha_2$, where $\alpha_1 = \exp(-\alpha_{01}L_1/2)$ is the electric-field transmission coefficient for the length L_1 between coupling regions 1 and 2, and $\alpha_2 = \exp(-\alpha_{02}L_2/2)$ is the electric-field transmission coefficient for the length L_2 between coupling region 2 and before region 1. The constants α_{01} and α_{02} are the optical power loss per unit length for the regions L_1 and L_2, respectively. The refractive index of the resonator is n_d. Finally, the round-trip time of the disk is $\tau = \tau_1 + \tau_2$, where $\tau_1 = n_\mathrm{d}L_1/c$, and $\tau_2 = n_\mathrm{d}L_2/c$. The self-consistent relations between field amplitudes at a time t for the two coupling regions are

$$B_1(t) = (1-\kappa_1^2)^{1/2}A_1(t) + \mathrm{i}\kappa_1 A_2(t)$$

$$B_2(t) = \mathrm{i}\kappa_1 A_1(t) + (1-\kappa_1^2)^{1/2}A_2(t)$$

$$D_1(t) = \mathrm{i}\kappa_2 C_2(t)$$

$$D_2(t) = (1-\kappa_2^2)^{1/2}C_2(t)$$

while optical propagation between coupling regions give

$$C_2(t) = \alpha_1 \mathrm{e}^{-\mathrm{i}\phi_1(t)}B_2(t-\tau_1)$$

$$A_2(t) = \alpha_2 \mathrm{e}^{-\mathrm{i}\phi_2(t)}D_2(t-\tau_2)$$

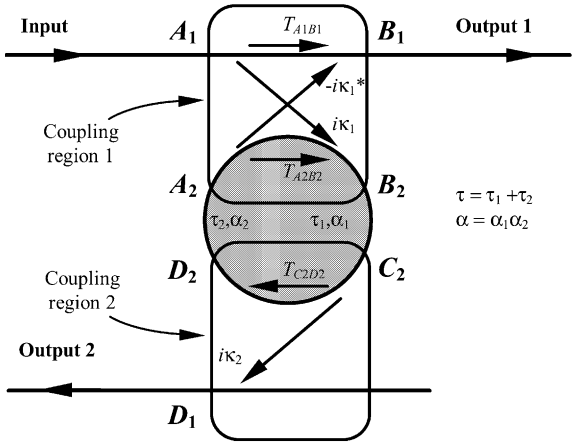

Fig. 5. Directional coupler model used to understand coupling principles of a microphotonic modulator. Photons incident on the input directional coupler are evanescently transferred into a ring or disk. After traveling around the disk, light is evanescently coupled out of the resonator at either output 1 or output 2. T_{ij} is the electric-field transmission coefficient of the coupling region, κ_i is the electric-field coupling coefficient of the coupling region, and α_i is the electric field transmission coefficient between coupling regions. Coupler losses are ignored.

Where $\phi_1(t)$, and $\phi_2(t)$ are the electrically induced optical phase shift along lengths L_1 and L_2. Using recursion and assuming a monochromatic input, the total output field from coupling region 1, $E_{\text{out1}}(t) \equiv B_1(t)$ as a function of the field input to coupling region 1, $E_{\text{in}}(t) \equiv A_1(t)$ then $E_{\text{in}}(t - p\tau) = E_{\text{in}}(t)\,\mathrm{e}^{-\mathrm{i}\omega p\tau}$, and

$$E_{\text{out1}}(t) = \left[\sqrt{1-\kappa_1^2} - \frac{\kappa_1^2}{\sqrt{1-\kappa_1^2}} \sum_{p=1}^{\infty} \rho_1^p \exp\left(\mathrm{i}\sum_{q=0}^{p-1}[\phi_1(t - \tau_2 - q\tau) + \phi_2(t - q\tau)]\right)\right] E_{\text{in}}(t)$$

$$\rho_1 \equiv \alpha\sqrt{1-\kappa_1^2}\sqrt{1-\kappa_2^2}\,\mathrm{e}^{\mathrm{i}\omega\tau}$$

where ω is the optical frequency. Similar to the above method, recursion is used to find the total electric-field output from coupling region 2, $E_{\text{out2}}(t) \equiv D_1(t)$ as a function of $E_{\text{in}}(t)$. This gives

$$E_{\text{out2}}(t) = \left[-\kappa_1\kappa_2\alpha_1\,\mathrm{e}^{\mathrm{i}(\omega\tau_1+\phi_1(t))}\left(1 + \sum_{p=1}^{\infty}\rho_2^p \exp\left(\mathrm{i}\sum_{q=0}^{p-1}[\phi_1(t-(q+1)\tau) + \phi_2(t - \tau_1 - q\tau)]\right)\right)\right] E_{\text{in}}(t)$$

$$\rho_2 \equiv \alpha\sqrt{1-\kappa_1^2}\sqrt{1-\kappa_2^2}\,\mathrm{e}^{\mathrm{i}\omega\tau}$$

RF modulation frequency of the microphotonic resonator is determined by the FSR of the optical resonator

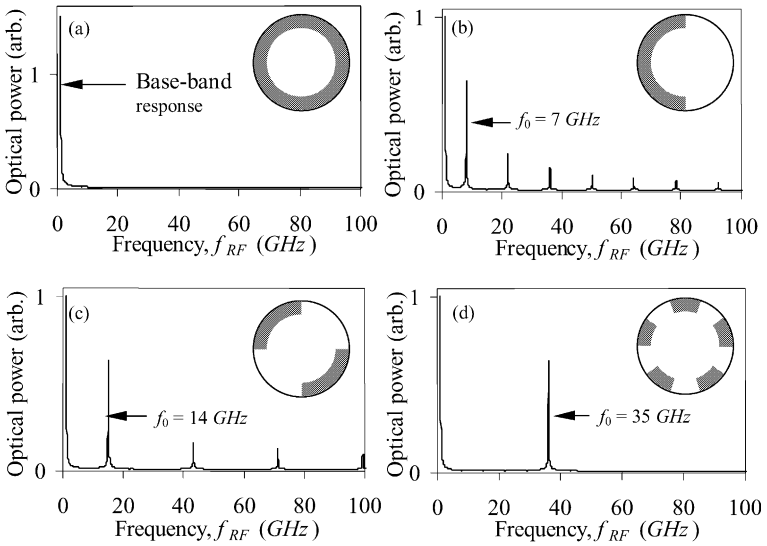

Fig. 6. Calculated response of a microphotonic-based opto-electronic modulator with the indicated periodic metal electrode structures. (a) A $R = 3.18$ mm $LiNbO_3$ disk modulator with $\kappa = 0.05$ and a continuous ring electrode. (b) $\kappa = 0.05$ with a split 2-segment ring-electrode showing resonant opto-electronic response at 7 GHz. (c) $\kappa = 0.05$ with 4 segments and response at 14 GHz. (d) $\kappa = 0.05$ with 10 segments showing response at 35 GHz.

and the spatial pattern of the metal electrode structure. The frequency of the RF carrier f_{RF} should be an integral multiple m of the optical FSR, f_{FSR}, where $f_{FSR} = 1/\tau_{disk} = c/(n_{opt}2\pi R)$, τ_{disk} is the optical round-trip time of the disk, and R is the disk radius [12]. A periodic metal electrode structure permits operation of the modulator well beyond a typically 20 GHz −3 dB roll-off of conventional commercial $LiNbO_3$ modulators.

As shown in Fig. 6(a) for a resonant solid-ring electrode, high optical-Q results in a summation of multiple round trips that further suppresses modulation efficiency at finite frequency. Fig. 6(b)–(d) illustrates how a change in the metal electrode pattern shifts the resonant response to higher frequencies with little decrease in efficiency.

The relative response at the resonant frequency compared to base band is 0.63 indicating the potential for efficient modulation. A larger modulation response at base-band results because a photon will encounter a larger average electric field during a single round trip. This is because the time constant determining this response is the round trip time $\tau_{disk} = 1/f_{FSR}$ of the disk.

Fig. 7(a) plots the optical power for the split 2-segment electrode case shown in Fig. 6(b) on a logarithmic scale. RF detected power would be two times optical power on this log scale. Fig. 7(b) and (c) shows expanded views of the optical modulation response at base band and fundamental disk frequency. Qualitatively, the presence of modulation dips result from spectral filtering by the optical resonance of the optical modulation side bands.

Fig. 8 qualitatively explains the presence of the dips. At base band for a fixed RF power and frequency f_{RF}, modulated optical power will be coupled out of the optical carrier frequency $f_{opt} = c/\lambda_{opt}$ and into optical side bands $f_{opt} \pm f_{RF}$. All three optical frequencies, f_{opt} and $f_{opt} \pm f_{RF}$, must be resonant within the disk to propagate.

Both experiment and simulation have verified that maximum modulation occurs near the maximum slope of the CW optical resonance, labeled in Fig. 7(a) as λ_{opt}. The base-band modulated response for the $\kappa = 0.05$ split 2-segment ring-electrode of Fig. 6(b) is shown in Fig. 7(b).

As f_{RF} increases, the optical side bands are modified according to the optical resonance peak. The approximate condition for maximum modulation occurs when one optical side band is aligned with the resonance peak ($f_{RF} = f_2$ in the figure). In the simulation, the optical input wavelength λ_{opt} was centered above the resonant wavelength such that $\Delta f = f_{peak} - f_{opt} = 50$ MHz.

In agreement with this qualitative description, simulated maximum modulation occurs at 54 MHz. The dip at 7 GHz is understood through a similar argument, where side bands are shifted by plus and minus one FSR into adjacent resonances. The peaks at 7 GHz occur ±4 MHz from the 7 GHz dip. Fig. 7(d) demonstrates the null in modulation when excited at the second harmonic

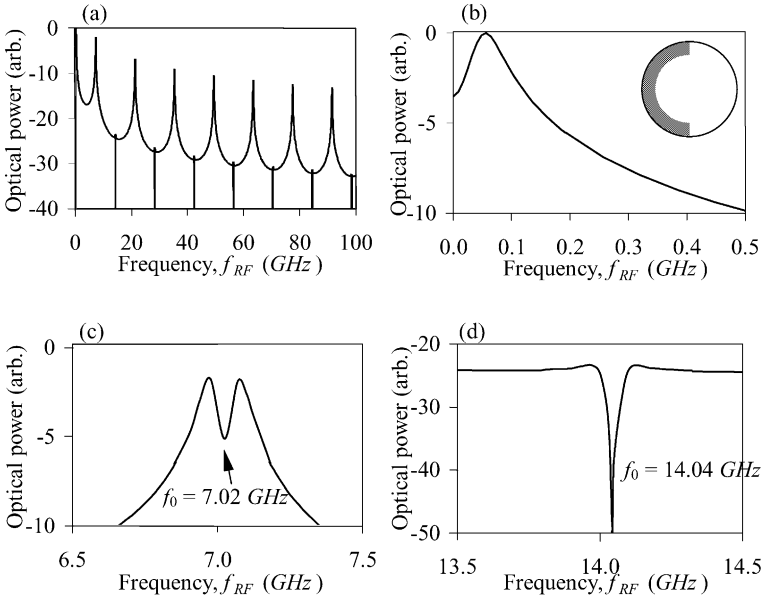

Fig. 7. (a) Calculated response of the $\kappa = 0.05$ with split 2-segment ring-electrode of Fig. 6(b) shown using a log scale. (b) Expanded view of the base-band response. (b) Expanded view of the fundamental 7 GHz modulation response showing a modulation dip at the center of the modulation peak. (d) Expanded view at 14 GHz showing a null in modulation at the second harmonic.

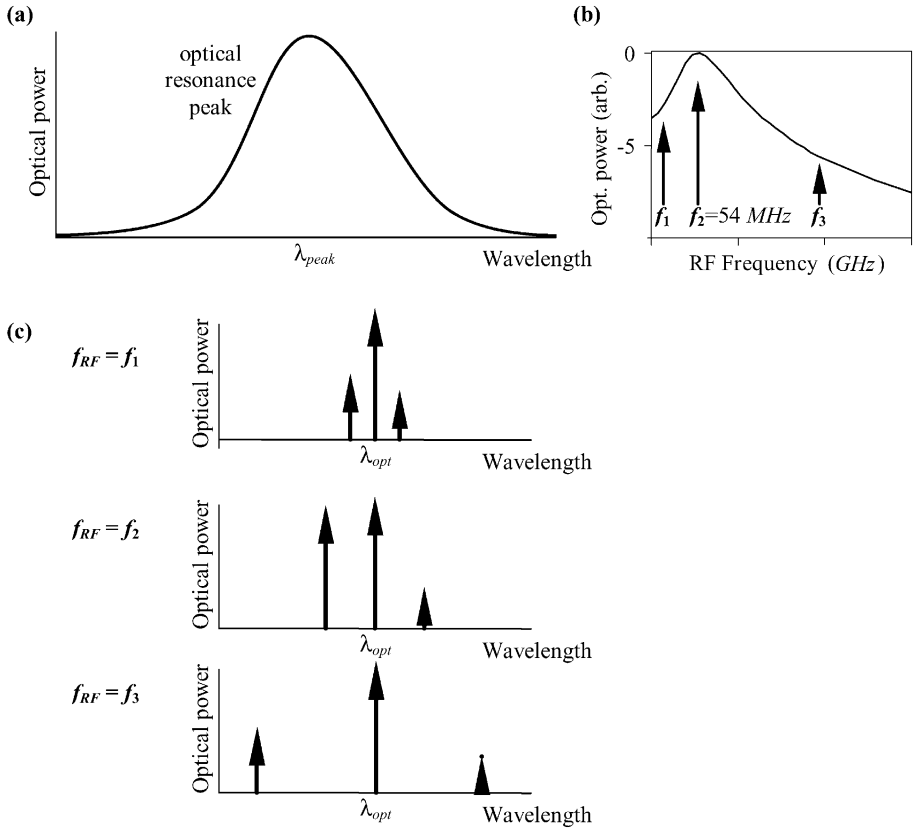

Fig. 8. (a) CW optical resonance peak centered at wavelength λ_{peak}. (b) Optical modulation response as a function of applied RF frequency for the two-section electrode in Fig. 6(b). (c) Optical carrier and side-band wavelengths for the three indicated RF frequencies shown in part (b). The amplitude of each wavelength is optically filtered by the resonance peak. Therefore $f_{RF} = f_2$ will have the maximum modulation as shown in (b).

frequency. This results when light passing between the electrode is modulated at the second harmonic of the total round trip frequency. In this case, the total phase shift from the electrode is zero, and there is no modulation.

2.3. The role of the reference arm

Both experiment and simulation have shown that the reference arm in Fig. 4(a) is not always necessary, and the configuration shown in Fig. 4(b) can be used to achieve efficient modulation. For a single coupler configuration ($\kappa_2 = 0$), Fig. 9 shows as the coupling coefficient decreases, a point is passed where the Mach–Zehnder geometry is no longer needed.

Amplitude modulation is achieved through a combination of two mechanisms. In the first, phase-shifted light exiting the active arm of the Mach–Zehnder interferes with light in the reference arm, thereby converting phase information to amplitude modulation. In the second mechanism, because light of increasing round-trip number has a larger accumulated phase shift, amplitude modulation will result due to interference

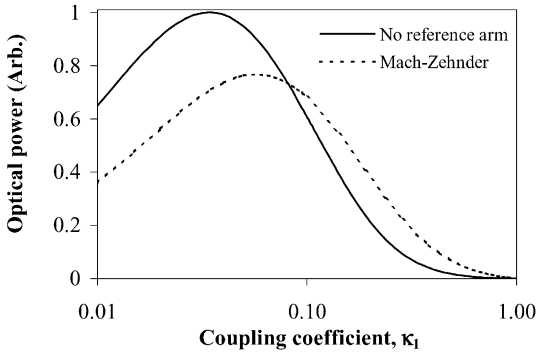

Fig. 9. Simulated comparison of modulation with and without use of a Mach–Zehnder geometry using the single-coupler geometry. Amplitude modulation without the Mach–Zehnder is shown to result in larger modulation at coupling coefficients $\kappa_1 < 0.085$. Values used in the simulation are the same as those in Fig. 6(b).

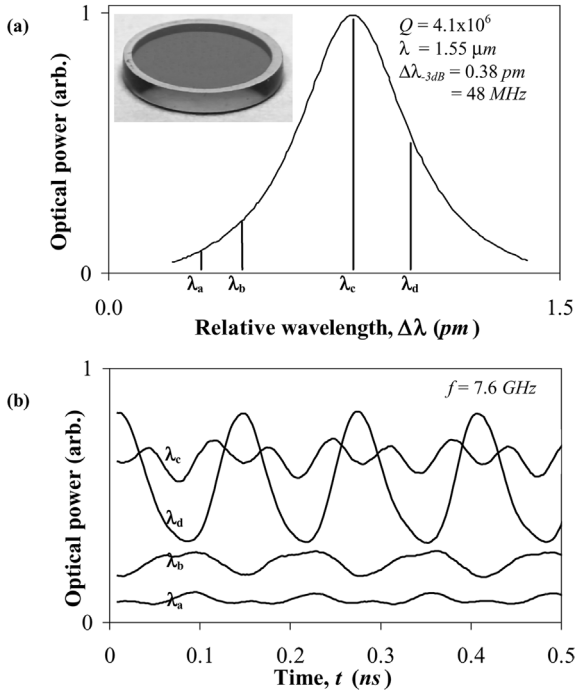

Fig. 10. (a) Measured optical resonance of the $LiNbO_3$ microphotonic disk modulator near wavelength $\lambda = 1.55$ μm. The measured Q of this device is more than 4×10^6. Inset shows a photograph of a z-cut $LiNbO_3$ disk-shaped resonator with optically polished curved side walls. Gold electrodes are placed in an annulus around the disk to increase the overlap of electrical bias and optical fields. The dimensions of the disk are radius $R = 2.92$ mm and thickness $d = 0.74$ mm. (b) Detected optical time-domain signal showing 7.56 GHz modulation. Modulation is shown at four wavelengths referenced in (a), and is maximum at a wavelength corresponding to the maximum slope of the optical resonance.

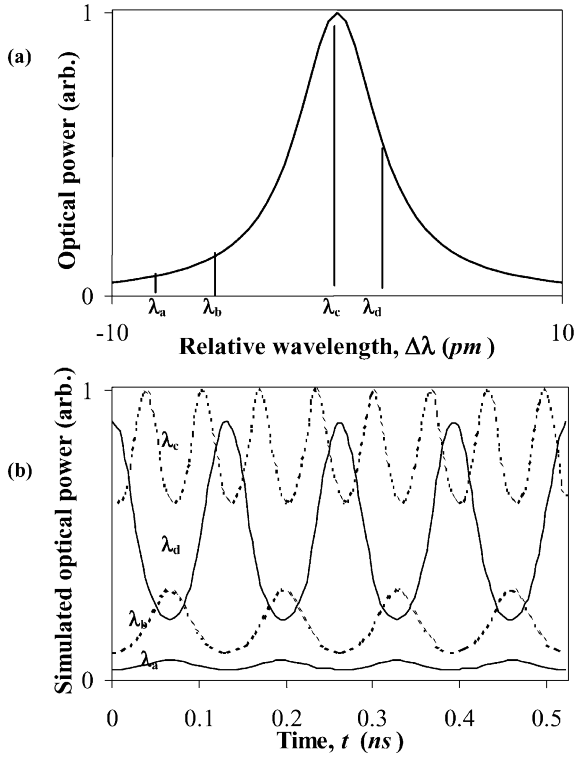

Fig. 11. (a) Simulated optical resonance of the $LiNbO_3$ microphotonic disk modulator near wavelength $\lambda = 1.55$ μm. The radius of the disk is $R = 2.92$ mm. (b) Simulated optical time-domain signals showing 7.6 GHz modulation. Modulation is shown at four wavelengths referenced in (a), and is maximum at a wavelength corresponding to the maximum slope of the optical resonance.

between individual round trips. Because each round-trip optical path length is an integral multiple of the optical wavelength, this "self-modulation" is inherently phase matched.

Fig. 9 shows a comparison of modulation with and without the Mach–Zehnder geometry. In a single pass limiting case $\kappa_1 = 1$ and $\kappa_2 = 0$, light passing along the active arm is phase modulated. It is then amplitude modulated via interference with light from the reference arm. Because there is only one round trip, there is no self-modulation. As κ_1 decreases from 1, self-modulation becomes a larger fraction of the total modulation, and amplitude modulation via the Mach–Zehnder mechanism becomes less important. Below a value of $\kappa_1 = 0.085$ in the simulation, the Mach–Zehnder geometry is disadvantageous, and a modulation geometry without the reference arm is more efficient. Hence, microphotonic modulators with small values of κ_1 are best implemented without use of a reference arm (see Fig. 4(b)).

Comparison of experiment and simulation shows the typical coupling coefficients are $\kappa_1 < 0.05$, and therefore using a single-arm non-Mach–Zehnder configuration results in a more efficient modulation geometry. This more efficient and less complex experimental configuration is used for all experimental results presented here.

2.4. Comparison of calculated and measured modulation response

Fig. 10(a) shows the measured optical spectrum of the WGM resonance in the absence of RF modulation, with a resulting optical $Q = 4 \times 10^6$. As shown in Fig. 10(b), measured optical modulation in the time domain is maximized for a fixed RF input power when the optical wavelength λ_d is located at the maximum slope of the WGM spectral shape. Frequency doubling is shown to occur at the wavelength λ_c at the center of the optical resonance. In addition, because the slopes are opposite

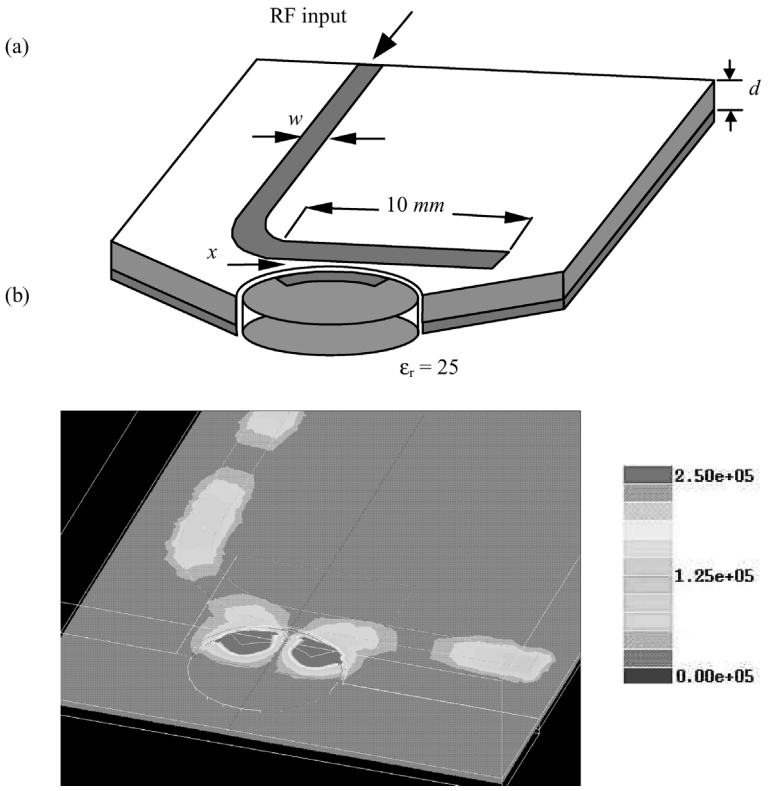

Fig. 12. (a) Side-coupled resonator geometry used to achieve simultaneous resonance with RF voltage gain. (b) Simulation results showing the RF intensity at the fundamental frequency of the RF resonator. The simulation assumed a dielectric thickness, $d = 0.508$ mm, relative dielectric constant, $\varepsilon_r = 2.94$, line width, $w = 1.2$ mm, disk thickness, $t = 0.7$ mm, resonator width = 1.2 mm, resonator angle = 90°, and gap spacing, $x = 0.3$ mm. Scale is in arbitrary linear units.

on either side of the optical resonance, the modulation response at λ_c and λ_d are π out of phase.

As additional confirmation of the microphotonic resonator modulation model, time domain simulation is compared to the experimental data shown in Fig. 11. Fig. 11 shows very good agreement with the experimental data in Fig. 10, including frequency doubling, the π phase change, and maximum modulation occurring near the maximum slope of the optical resonance.

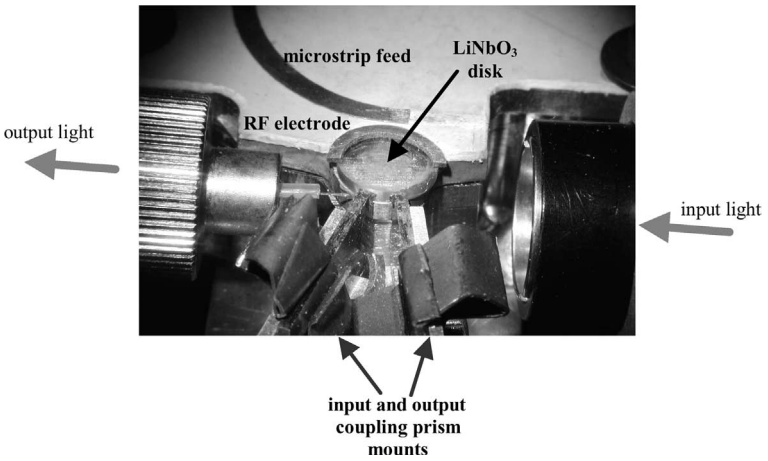

Fig. 13. Photograph showing the experimental setup used for the side-coupled electrode coupling scheme.

3. RF modulation experiments at mm-wave frequencies

3.1. Side-coupled electrode coupling

A side-coupled microstripline resonator is used to achieve both voltage amplification and efficient RF coupling to the microphotonic resonator electrode. Fig. 12(a) shows the geometry of the side-coupled electrode. A SMA launch is used to couple power from the RF source to a microstrip line of 50 Ω impedance patterned on a RT-Duroid 6002 substrate with $\varepsilon_r = 2.94$. Simulation shows that RF power reflects from the open end of the microstrip line generating the standing wave pattern seen in Fig. 12(b). However, part of the RF power evanescently couples to a microstrip resonator of length L that is either patterned or placed on the $LiNbO_3$ disk. This coupled power generates standing waves at RF frequencies $f_{RF} = mc/(2n_{eff}L)$, where n_{eff} is the effective RF index of refraction seen by the RF mode, and m is an integer. Fig. 12(b) shows RF intensity of a simulated resonant standing wave.

Fig. 13 shows the RF and optical experimental configuration. Prisms are used to couple laser light of approximate wavelength $\lambda = 1.55$ μm into and out of the WGM optical mode of the microphotonic resonator. The optical wavelength is tuned to a resonant wavelength of the optical resonator. A RF electric field propagating on a 50 Ω impedance metal microstrip line evanescently side couples to a metal electrode resonator on the $LiNbO_3$ disk. The fundamental resonant frequency of the electrode resonator is tuned to match the optical FSR of 7.56 GHz.

3.2. Experimental results of mm-wave modulation

Demonstration of mm-wave modulation in the $LiNbO_3$ microphotonic resonator using simultaneous RF and optical resonance with voltage gain on the RF electrode is shown in Fig. 14(a). Optical modulation is demonstrated in the Ka band at 30.3 GHz. By side coupling a 30.3 GHz RF signal into the third harmonic of a 10.1 GHz RF microstrip resonator, optical modulation at 30.3 GHz is achieved. Fig. 14(b) shows only residual modulation when the optical wavelength is tuned-off resonance, while the RF frequency is still set to resonance. Fig. 14(c) shows the optical wavelength on resonance, with the RF frequency tuned-off resonance.

Using a similar experimental arrangement, optical modulation at 37.9 GHz has also been demonstrated as shown in Fig. 15. This modulation used the third harmonic of a 12.6 GHz microstrip resonator for RF coupling to the metal electrode.

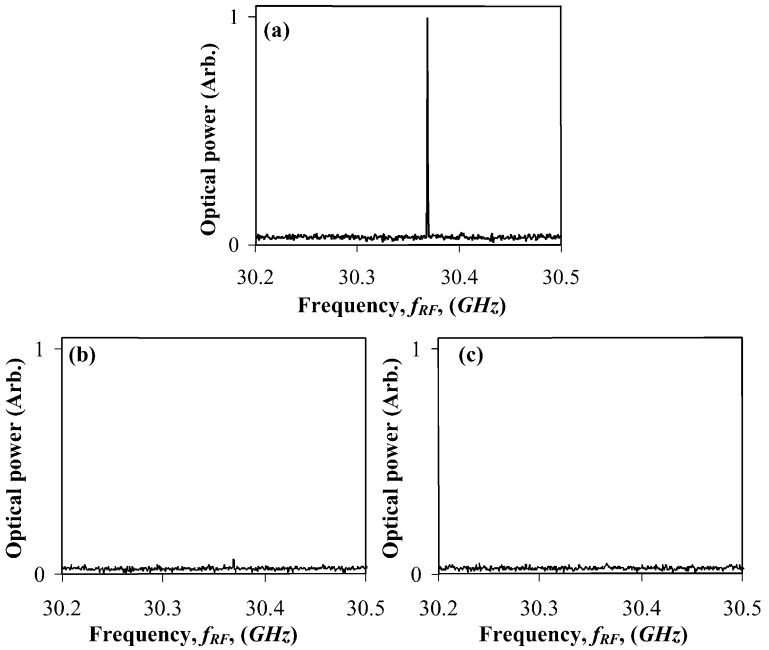

Fig. 14. (a) Demonstration of mm-wave modulation at 30.37 GHz using a $LiNbO_3$ microphotonic resonator with both the RF frequency and optical wavelength tuned to resonance. (b) When the optical wavelength is tuned-off resonance, while the RF frequency stays in resonance, no modulation is measured. (c) No modulation is observed if the optical wavelength is kept tuned on resonance while the RF frequency is tuned-off resonance.

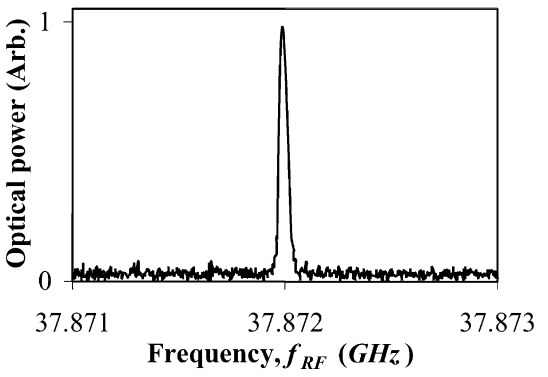

Fig. 15. Measured modulation response of a $LiNbO_3$ microphotonic resonator at 37.9 GHz. RF resonance was achieved using the third harmonic of a 12.6 GHz microstrip resonator.

4. Conclusion

Theory and simulation for a new type of mm-wave RF modulator with direct electrical-to-optical conversion has been discussed. Simulation shows very close agreement with experimental results at GHz frequencies and confirms our model. In addition, experimental modulation of a RF carrier using a side-coupled RF coupling scheme has demonstrated modulation at frequencies approaching 40 GHz.

Acknowledgements

This work is supported in part by NSF under contract ECS-9979331 and the DARPA RFLICs program.

References

[1] Ohata K, Inoue T, Funabashi M, Inoue A, Takimoto Y, Kuwabara T, Shinozaki S, Maruhashi K, Hosaya K, Nagai H. IEEE Trans Microwave Theory Technol 1996;44:2354.
[2] Cohen DA, Levi AFJ. Electron Lett 2001;37:37.
[3] Cohen DA, Levi AFJ. Solid-State Electron 2001;45:495.
[4] Cohen DA, Hossein-Zadeh M, Levi AF. J Electron Lett 2001;37:300.
[5] Robertson WM, Arjavalingam G, Kopcsay GV. Electron Lett 1991;27:175.
[6] Stratton JA. Electromagnetic theory. New York: McGraw-Hill; 1941.
[7] Reitz JR, Milford FJ, Christy RW. Foundations of electromagnetic theory, third edition. New York: Addison-Wesley, 1980.
[8] Frateschi NC, Levi AFJ. J Appl Phys 1996;80:644.
[9] Little BE, Laine JP, Haus HA. J Lightwave Technol 1999; 17:704.
[10] Kight JC, Dubreuil N, Sandoghdar V, Hare J, Lefevre-Seguin V, Raimond JM, Haroche S. Opt Lett 1995;20: 1515.
[11] Gorodetsky ML, Ilchenko VS. Opt Commun 1994;113: 133.
[12] Kourogi M, Nakagawa K, Ohtsu M. IEEE J Quantum Electron 1993;29:2693.